Fundamental research on the voltammetry of polycrystalline gold

Yang, S.


Forms of
Electric Charge
Energy Conversion
Energy Storage
复杂背后的本质是简单。
The essence behind complexity is simplicity.

4

Exploring the excess free charge distribution under catalytic conditions using a quartz crystal microbalance methodology

Abstract

Understanding the distribution of the excess free charge at electrified interfaces is pivotal for the development of various energy conversion systems, such as electrolysers and fuel cells, and energy storage systems including electrical double layer capacitors, pseudocapacitors and batteries. Nonetheless, measuring the excess free charge on a solid material directly is challenging. This study introduces the utilization of an electrochemical quartz crystal microbalance (EQCM) as an innovative approach to discern and quantify the electrode excess free charge. The EQCM exploits the oscillation frequency of a quartz crystal as a sensitive indicator of mass changes on a gold electrode. By capitalizing on the frequency response of the quartz crystal to the electrostatic attraction of free charges, this method may provide a means to identify the potential regions where a positive and a negative excess charge exist, respectively. Our study reveals the presence of a potential region where no frequency changes can be detected by EQCM, while an increase in $-\Delta f$ occurs on both sides of this region. Under the assumption that the $-\Delta f$ reflects the complete formation of excess charge, our EQCM methodology allows for identification and quantification of the excess charge even during the catalytic oxygen reduction reaction. Through a comparison of the frequency response recorded by the EQCM and the capacitance recorded by cyclic voltammetry, we can estimate the amount of excess free charge and the Faradaic charge in the entire pH scale. Furthermore, by examining the correlation between the excess free charge and the frequency response, we have constructed excess free charge distribution diagrams for both Ar and O_2 saturated solutions.These diagrams aim to visually depict how the excess charge may fluctuate at specific pH levels and applied potentials before and during catalysis.

4.1 Introduction

When an electrode is immerged into an electrolyte solution and a potential is applied, an excess free charge (either positive or negative) will emerge on the electrode surface and attract ions with an opposite charge. The precise structure of this electrified interface plays a crucial role in various energy-conversion systems such as chemical energy conversion systems (e.g. water splitting, fuel cells), and electrochemical energy storage devices (e.g. electrical double layer capacitors, pseudocapacitors, batteries).[1-6] The presence of a potential of zero charge (PZC) is a defining characteristic of the interfaces of all these systems, representing the potential at which no excess charge exists on the electrode surface.[7-9] Initial insights into the excess free charge and the PZC were gained from measurements of the surface tension at the mercury-electrolyte interface, where the PZC is pinpointed as the potential corresponding to the maximal surface tension on an electrocapillary curve.[2, 10] Surface tension measurements were deemed as a direct approach for detecting the excess free charge on liquid metal surfaces.[11] However, extending such surface tension measurements to a solid material remains impossible. Drawing motivation from the successful identification of the PZC at mercury, which divides the electrified interface into two areas with opposing excess free charges, several indirect techniques have been developed to determine the PZC in solid materials. These methodologies encompass differential capacitance measurements,[10, 12] the CO charge displacement method,[13, 14] laser-induced temperature-jump methods,[15, 16] probe molecules techniques,[17, 18] spectroscopy methodologies,[19, 20] and computational approaches.[1, 5, 7] However, all these indirect techniques become inapplicable in determination of the PZC when specific adsorption reactions accompanied with charge transfer occur simultaneously— an occurrence widespread in solid materials.[21]

Exclusion of such chemisorption effects are for example important in the determination of the PZC with the minimum differential capacity approach, wherein it is assumed that the PZC is located there where the capacitance is minimal. Here any Faradaic current resulting from chemisorption reactions will directly disrupt the calculation of the differential capacity that relies on non-Faradaic current measurements. Increasingly intricate physical-chemical models have been integrated into the classical Couy-Chapman-Stern (GCS) model, that for example

include the field-dependent arrangement of water molecules, the discrete nature of adsorbed ions, and the quantum behavior of metals.[2, 22, 23] Consequently, it is often possible to achieve a perfect fit for many capacitance profiles, by simply adjusting the model parameters. It is however imperative to corroborate these assumptions through precise experimental investigations.

Other indirect methods to measure the PZC also exhibit limitations in determining the PZC in the presence of chemisorption reactions taking place. Determination of the PZC by laser-induced temperature-jump methods relies on monitoring of the orientation of interfacial water. However, this approach is ill-suited for situations involving chemisorption, as chemisorbed species hinder the reorientation of such water molecules.[15, 16] Probe molecule approaches, in which catalytic reactions are monitored that are sensitive to electrolyte accumulation, are sometimes employed to determine the PZC. Yet these methods are problematic given that the introduction of a chemical reagent that reacts with the electrode surface, and alters the electrochemical driving force for the forward chemical reaction during the analysis. This makes it challenging to accurately determine the PZC.[17, 18] While spectroscopic methods can offer valuable insights into the type of ions that are present and how these interact with the electrode interface, determination of the PZC remains highly challenging, given that spectral changes might not always directly correlate with variations in the excess free charge. Moreover, extracting meaningful information from obtained spectra often requires advanced data analysis and modeling techniques.[19, 21]

It is crucial to highlight that the excess free charge density, rather than the electrode potential, directly governs the strength of the interfacial electric field.[24, 25] This electric field in turn influences the energy of the bonds formed between the electrode surface and adsorbates.[24] Specifically the orientation of interfacial water,[5, 26, 27] and the hydration state of ions at the interface,[28, 29] strongly depend on the excess free charge density. Therefore determining the excess free charge is important for understanding the reaction pathways and energetics occurring at the solid-liquid interface of electrodes.[30-32] Due to the absence of an appropriate in situ method to quantify the excess free charge density, most research in this area has focused on identification of the PZC rather than exact measurements of the excess charge to monitor

the excess free charge distribution.[7, 19, 24] Thus far it has remained particularly challenging to pinpoint how the charge distribution occurs at the electrode surface when specific adsorption reactions comes into play. This particularly holds when electrochemical reactions occur simultaneously with the buildup of excess charge as is typical in real environments. Under such conditions very little is known on how the excess free charge changes as a function of the applied potential. This question is the source of contentious issues within energy conversion systems, such as the extensive discussions on the role of electrolytes and solvents in electrocatalytic processes in chemical energy conversion[33-35] as well as the intricate charge storage mechanisms in the field of electrochemical energy storage.[36-38]

Motivated by the necessity for a direct method to measure the excess free charge within practical electrochemical environments, we introduce the application of an electrochemical quartz crystal microbalance (EQCM) to identify and quantify the electrode charge. The proposed EQCM method may offer a means to identify the electrode charge, thereby allowing one to shed light on the intricate interplay between the excess free charge and electrochemical processes.

4.2 Experimental results

4.2.1 Direct determination of excess free charge on EQCM

EQCM is a sensitive technique that relies on an oscillating piece of quartz which frequency of oscillation relates to the mass of the piece of quartz. In the EQCM configuration, an ultrathin gold layer – on top of the piece of quartz – functions as a working electrode (Fig. 1). During electrochemical measurements frequency alterations triggered by mass changes at the electrode surface can be detected. In principle, these frequency changes can be converted to mass changes via the Sauerbrey equation: $\Delta m = C_f \cdot (-\Delta f)$.[39, 40] At the liquid – solid interface, alterations in frequency may not only originate from actual changes in mass of the solid electrode, but also in fluctuations of the density or viscosity of the electrolyte in the near vicinity of the electrode.[41-43]

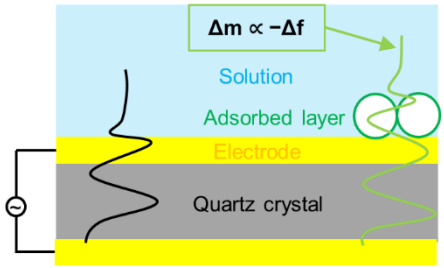

Fig. 1 EQCM setup illustrating the measurement of adsorbed molecule mass by tracking the resonant frequency change of a quartz crystal.

Initially, EQCM was primarily employed to detect Faradaic electrochemical deposition and striping processes.[39, 44] However, consistent frequency responses were even found in the regions of the electrochemical double layer (EDL) where Faradaic processes were absent.[45-47] For example, the Aurbach group investigated the effect of a range of different electrolytes on the frequency response in a series of EQCM measurements.[46] They calculated the amount of the adsorbed ions (ΔΓ) from the frequency response in EQCM measurements. It was found that ΔΓ is sensitive to the type of cations and increases as the scanning potential decreases providing that the applied potential is set below the PZC. Yet ΔΓ is sensitive to the type of anions and increases as the scanning potential increases when the applied potential is set higher than the PZC. These observations clearly show that EQCM can be used to detect the accumulation of ions at different potential regions. We have also assessed the frequency response by varying cations and anions on the gold electrode in pH 3 solutions (Fig.2). The results distinctly indicate that the frequency change is responsive to the types of cations in a low potential range (Fig. 2A) and to the types of anions in a high potential range (Fig. 2B). Our findings on gold align with the EQCM experiments on nonporous carbon conducted by Aurbach group. These observations validate that the frequency response is indeed induced by the electrostatic adsorption of different ions, driven by the excess charge on the surface. Despite the many studies have explored in-situ monitoring of changes in the electrochemical double layer structure through EQCM,[42, 45, 46] there remains a notable gap in our understanding of the distribution of ions at the solid liquid interface in a real environment. Although it has been shown that the frequency changes relate with the excess free charge, we

still do not exactly know which precise phenomenon is responsible for the frequency change. For example, an increase of excess free charge may lead to an increase of the viscosity of solution and/or concentration of the electrolyte near or at the electrode surface, and a combination of all these effects may be picked up by the EQCM experiment. Solving this knowledge gap is further complicated given that the chemical society still knows very little about the precise chemical processes occurring at the electrode interface, and how these are affected by subtle changes in electrolyte composition and pH changes.. For instance, the specific location where ion chemisorption occurs, the precise nature of the chemisorption processes, and how chemisorption reactions vary with alterations in the solution environment including the type and concentration of electrolyte types and the pH have not been identified for most electrode surfaces.. In this study, we have further investigated the direct resonant frequency response of the quartz crystal that results from the electrostatic interaction of the excess free charge in relation to the pH, and the counterions that are present in solution in case of a gold electrode.

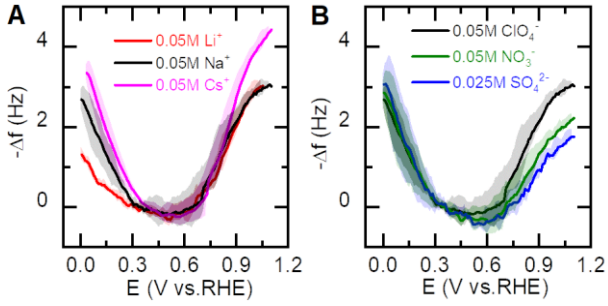

Fig. 2 the frequency change (-Δf) of EQCM on the gold electrode with change of types of ions at pH 3 solutions. (A) The frequency change (-Δf) at electrolytes with different cations. Anions is 0.05 M ClO_4^-. (B) The frequency change (-Δf) at electrolytes with different anions. Cations is 0.05 M Na^+. The shaded areas represent the range of frequency variations at every electrolyte during positive and negative scans in the three experiments.

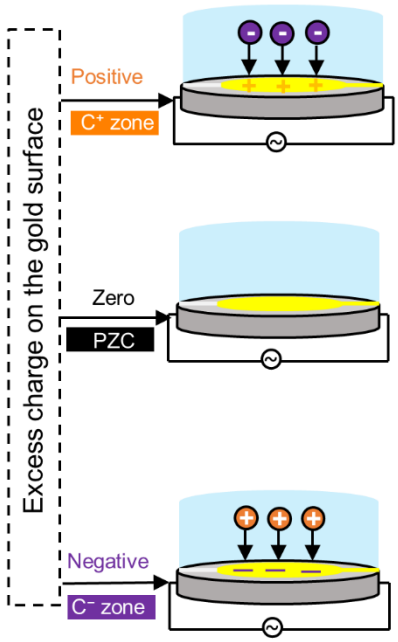

Fig. 3 Three proposed models depicting excess charge variations with a changing applied potential. When the surface possesses a positive charge, the quantity of the adsorbed anions corresponds to this positive excess charge. The associated potential region is termed the "C^+ zone". When the excess free charge remains at zero, no ions are electrostatically attracted, resulting in a potential of zero charge referred to as the "PZC". Conversely, when surface bears a negative charge, the amount of attracted cations corresponds to the negative excess charge. The corresponding potential region is labeled as "C^- zone".

In a hypothetical EQCM experiment there are three possible responses and related potential regions that one may expect to encounter (Fig. 3). The C^+ zone, the PZC, and C^- zone represent the potential regions, where a positive excess charge, zero excess charge and a negative excess charge exist, respectively. In order to establish a direct linear relationship between the excess charge and the frequency response, it is essential to first identify the correct C^+ and C^- zones.

As previous reports indicate, the chemisorption of anions frequently occur within the anticipated potential range where the PZC is expected.[20, 48, 49] Additionally, the potential region wherein the chemisorption of anions occurs is sensitive to various factors such as the electrolyte

type and concentration, as well as the pH. Cyclic voltammetry (CV) experiments on gold reveal two redox waves, which presence merely depends on the pH (Fig. 4B). One redox wave (X) is mostly visible in acidic solutions, while the other redox wave (Y) is most prevalent in more alkaline conditions. It is important to note at the position where the X or Y redox waves can be observed no significant frequency changes were observed in EQCM measurements. Instead a significant increase in $-\Delta f$ can be observed both at more positive and more negative potentials from the X and Y redox couples, as illustrated in Fig. 4A and Fig. S11.

Based on the QCM result, we can make a estimation of the potential region for the C^- and C^+ zones, respectively. To explore the correlation between excess free charge and the frequency response of the EQCM, we calculated the integrated charge of a CV (ΔQ) and the corresponding negative frequency change ($-\Delta f$) within the C^+ zone, in 0.1 M $HClO_4$, where the C^+ zone is most pronounced (Fig. 4D). This analysis distinctly reveals a proportional linear relationship without an intercept between ΔQ and $-\Delta f$, signifying that $-\Delta f$ directly corresponds to changes in the excess free charge in the C^+ zone. Additionally, in the C^- zone in 0.1 M NaOH, an inversely proportional relationship without an intercept between ΔQ and $-\Delta f$ was observed, indicating that $-\Delta f$ directly corresponds to changes of the excess charge in the C^- zone as well. (Fig. 4C) Furthermore, we have calculated ΔQ at different potential windows and found that the linear relationship between ΔQ and $-\Delta f$ is disrupted at a potential where the redox couples X and Y can be observed (Fig. S4).

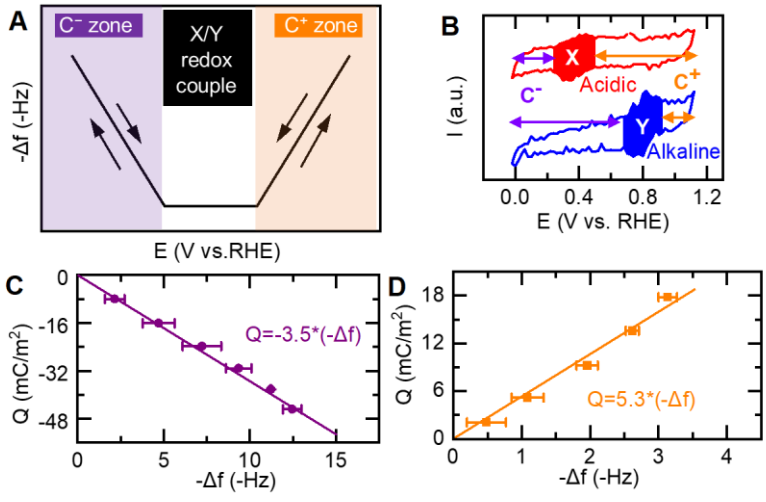

Fig. 4 Detection of the surface excess charge through electrochemical quartz crystal microbalance (EQCM) measurements. (A) Frequency response of the EQCM at various potential regions: $-\Delta f$ increases as the potential decreases in the C^- zone, but increases as the potential increases in the C^+ zone. Notably, there is a potential region where the X/Y redox reactions occur, effectively maintaining $-\Delta f$ at a minimum value. (**B**) Linear correlation of the frequency response and the integrated charge in the C^+ potential region in 0.1 M $HClO_4$. (**C**) Cyclic voltammograms (CVs) of gold in different Ar-saturated pH solutions at a scan rate of 50 mV/s. The C^+ and C^- zones denote the potential regions where a positive and negative surface excess charge is present, respectively. X and Y represent the regions where redox reactions occur in acidic (pH 3) and alkaline (pH 10) solutions, respectively. (**D**) Linear correlation of the frequency response and the integrated charge in the C^- potential region in 0.1 M NaOH.

In case of an ideal electrified interface, the capacitance (C) is constant irrespective of the scan rate. The change of the non-Faradaic charge (ΔQ) is related to the potential drop (ΔE) and C, and can be expressed as $\Delta Q = C \times \Delta E$.[4] Consequently, ΔQ remains independent of ν, even though the current (I) is proportional to ν ($I = C \times \nu$) while C remains constant.[38] To further confirm the direct relationship between the frequency change and the accumulation of the excess free charge, we investigated $-\Delta f$ at varying scan rates (ν) (Fig. S1). These experiments show that $-\Delta f$ is not affected by ν in both the C^+ and C^- zones, which fully in agreement with the expected behavior of a non-Faradaic process.

The classical GCS model divides the total capacitance of the electric double layer (C_{GCS}) into Helmholz capacitance (C_H) and the diffuse layer capacitance (C_{GC}):[10, 12]

$$\frac{1}{C_{GCS}} = \frac{1}{C_H} + \frac{1}{C_{GC}}$$

In this simplistic equation, C_H is assumed to remain constant, and C_{GC} is expected to decrease with lower electrolyte concentration.[50] Consequently, it is anticipated that the total capacitance will decrease at a lower electrolyte concentration. This decrease in electrolyte concentration directly leads to a decrease in the excess charge that is attracted to the surface in

line with the equation $\Delta Q = C \times \Delta E$. If the frequency change is indeed linked to the excess free charge, a diminishing $-\Delta f$ should logically manifest when the electrolyte concentration is lowered. To validate this hypothesis, we examined the impact of the electrolyte concentration on the frequency changes in the C^+ zone (Fig. S2A) and in the C^- zone (Fig. S2B). Indeed $-\Delta f$ diminishes in both zones when the electrolyte concentration is decreased from 0.1 M to 0.05 M. The diminished $-\Delta f$ observed in a more diluted solution further solidifies the direct relationship between the frequency change and excess charge on the gold surface.

4.2.2 Chemisorption of anions at the electrode surface

Under conditions that are thermodynamically favorable, solvated ions can undergo partial dehydration and engage in bonding interactions with the electrode surface. This phenomenon, termed partial charge transfer, can lead to the formation of partially charged chemisorbates.[51] This behavior has been observed primarily with anions on metallic surfaces due to their weakly bound solvation shells.[21] The two redox waves, denoted as X and Y, have previously been associated with chemical adsorption/desorption phenomena.[49, 52] (Fig. 5A). For instance, the X wave is linked to the chemisorption of anions such as perchlorate, sulfate and nitrate, while the Y wave involves the chemisorption of hydroxide. To understand these phenomena better, we examined the oxidation peak potentials (E_{X+}) and (E_{Y+}) (Fig. 5B) as well as the reduction peak potentials (E_{X-}) and(E_{Y-}) (Fig. 5C) in relation to the pH. This revealed that E_{X+} (0.31 V vs. NHE) and E_{X-} (0.19 V vs. NHE) are pH−independent on the NHE reference scale when the pH is below 8. On the other hand, E_{Y+} ($0.82\,V - 0.059\,V/pH\ vs.NHE$) and E_{Y-} ($0.77V - 0.059\,V/pH\ vs.NHE$) exhibit a pH−dependent shift of − 59 mV/pH in the pH range of 8 – 13.

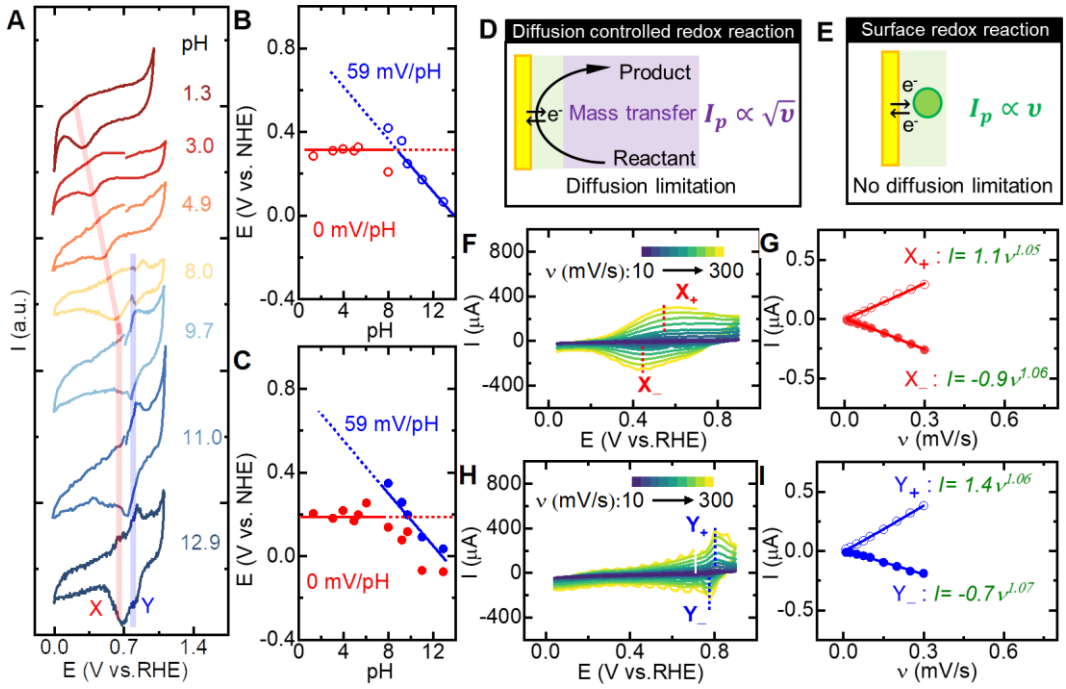

Fig. 5 X and Y redox peaks in the electrochemical double layer (EDL) region. (A) Cyclic voltammograms (CVs) of gold in Ar-saturated pH solutions (0.1 M ClO_4^-) at 50 mV/s. (**B**) Pourbaix diagram illustrating the X^+ (E_{X^+}) and Y^+ (E_{Y^+}) oxidation peaks during the positive scan of the CVs (Data from Fig. 5A). (**C**) Pourbaix diagram showcasing the X^- (E_{X^-}) and Y^- (E_{Y^-}) reduction peaks during the negative scan of the CVs (Data from Fig. 5A). (**D**) Schematic representation of a diffusion controlled redox reaction and its electrochemical response displaying the relationship between the peak current (I_p) and the square root of the scan rate ($\sqrt{\upsilon}$). (**E**) Schematic representation of a surface redox reaction and its electrochemical response demonstrating the relationship between the peak current (I_p) and the scan rate (υ). **(F)** CVs of gold in Ar-saturated 0.1 M $NaClO_4$ (pH 4) solutions at varying scan rates ranging from 10 to 300 mV/s. (**G**) Relationship between the scan rate and the X^+ and X^- peak currents in pH 4. (**H**) CVs of gold in Ar-saturated 0.1 M $NaClO_4$ (pH 10) solutions at varying scan rates ranging from 10 to 300 mV/s. (**I**) Relationship between the scan rate on the Y^+ and Y^- peak currents in pH 10.

The peak potentials associated with anion chemical adsorption and desorption (X redox couples) depend on the electrolyte concentration and the specific type of anion present (see S1

for details). Similar shifts in potential due to anion−dependent chemisorption (such as ClO_4^-, NO_3^-, or SO_4^{2-}) have been directly observed on the Au(111) surface using various in situ spectroscopy techniques, including surface-enhanced infrared absorption spectroscopy (SEIRAS), subtractive normalized interfacial Fourier transform IR spectroscopy (SNIFTIRS), IR reflection-absorption spectroscopy (IRAS).[20, 48, 49] Despite their relatively low surface coverage (less than 20%), the spectra clearly demonstrate that the bands corresponding to adsorbed anions (ClO_4^-, NO_3^-, and SO_4^{2-}) shift as the potential becomes more positive within the potential range where the X redox couple is active on Au(111). This direct evidence supports the notion that the X redox peaks are associated with direct anion binding to the gold surface.

As anticipated, the chemisorption of hydroxide is pH−dependent and shifts with a factor of $-0.059 \times pH$ in the Pourbaix diagram (Fig. 5B-C). While the detection of hydroxide absorption is typically easier in alkaline solutions,[52, 53] it can even be observed at pH 3 when the anion concentration is significatly reduced to 0.01M (Fig. S6 and S8). The Pourbaix diagram illustrates that the chemisorption potential of perchlorate shifts towards the chemisorption potential of hydroxide when the pH increases (Fig. 5B and C). The slope of E_{ClO4^-} ultimately changes from 0 mV/pH to −59 mV/pH once the pH surpasses 8, and the perchlorate and hydroxide chemisorption features closely overlap (Fig. 5 and Fig. S5-8). This change indicates a shift in anion chemisorption from an electron transfer (ET) process within the pH range of 1-8 to a proton−coupled electron transfer (PCET) process when the pH exceeds 8. This may suggest that co-chemisorption of perchlorate and hydroxide may occur within the pH range of 8-13, given their closely aligned equilibrium potential.

In the context of a redox reaction, the current response to an applied sweep rate (ν) hinges on whether the redox reaction process is governed by diffusion or surface phenomena.[54, 55] When a redox reaction is controlled by diffusion, the current response varies with the square root of the scan rate ($I_{(V)} = a\nu^{1/2}$) (Fig. 5D).[54, 56] Conversely, if a redox reaction is primarily constrained by surface reactions and not influenced by diffusion, the current exhibits a direct linear relationship with the scan rate ($I_{(V)} = a\nu$) (Fig. 5E).[38, 54] Since the concentrations of Na^+ and ClO_4^- are roughly the same at 0.1 M, both at pH 4 and at pH 10, these specific pH values were selected to examine the correlation between the peak currents (I) and the scan rate (ν), as

depicted in Fig. 5F and H. The data in Fig. 5G and 5I unmistakably indicate that the current responses I_X and I_Y are directly proportional to the sweep rates for both the negative and positive scans. Since both features associated with perchlorate and hydroxide chemisorption follow a relationship of $I_{(V)} = av$, it can be inferred that both processes are governed by surface-controlled reactions devoid of diffusion involvement. Such surface-controlled redox reactions are commonly referred to as pseudocapacitance due to their proportionality to the scan rate, resembling the behavior of a physical capacitor. However, unlike traditional capacitors, these process involve Faradaic currents, as they stem from the occurrence of redox reactions.[38, 54] Notably, these redox reactions involving anions (X) and hydroxide (Y) are not diffusion controlled, suggesting that the anions are already present at the interface, or in case of Y involve the solvent (water).

In the potential region where the X (acidic conditions) and Y (alkaline conditions) redox waves are observed, $-\Delta f$ is unaffected by ΔQ (Fig. S3 and S4). This finding suggests that the excess free charge may remain relatively constant during these redox reactions, even as the potential changes. While the classical GCS model clearly elucidates the behavior of excess charge on the surface in the absence of chemisorption, it remains unclear how excess charge evolves when chemisorption occurs. It is worth noting that detecting excess charge changes in the presence of chemisorption has been considered a challenging task.[8] EQCM may offer a promising perspective for observing how the excess charge changes in a real-world environment. In the electrochemical double layer (EDL) potential region, EQCM exhibits a pronounced frequency response when there is no chemisorption and a minimum frequency response when chemisorption is occurring. The Kautek group examined the frequency changes on the gold electrode using EQCM in 0.5 M KOH. They observed a minimum frequency response in the potential region that is associated with OH^- chemisorption but noted a significant frequency response both above and below this region.[42] Furthermore, they compared the frequency and mass difference at various potential regions, to study diverse electrochemical processes such as the specific adsorption of hydroxide, and structural changes in the double layer potential region. The Kautek group proposed double layer models involving the outer and inner Helmholz layers, based on the frequency responses on the gold surface observed by

EQCM measurements. They suggested that within the outer Helmholtz layer, fully solvated anions or cations exhibit electrostatic attraction/repulsion, which can be detectable through frequency changes on the EQCM in the EDL region. However, within the inner Helmholtz layer, where specific anions are adsorbed, the formation of neutral ion pairs with the metal surface may lead to practically no observable electrostatic attraction/repulsion.

The EQCM measurements demonstrate that $-\Delta f$ remains at a minimum, with no significant frequency changes occurring in the potential regions where the surface-controlled chemisorption reactions transpire, as illustrated in the X zone in Fig. 6A and B, and the Y zone in Fig. 6C. EQCM measurements enable the identification of the C^+ zone, C^- zone and PRMF across the entire pH scale, as illustrated in Fig. 6D. Jun Cheng's group reported state-of-the-art ab initio molecular dynamics simulations of electrified Pt(111)/water interfaces.[5] Their research revealed the existence of water chemisorption when the metal surface transitions from a negative to a positive charge. This chemisorbed water alters the surface coverage, subsequently increasing the differential capacitance, resulting in a bell-shaped differential capacitance curve. We speculate that a similar chemisorption behavior may also occur with anions in case of the gold electrodes of study when the excess free charge shifts from negative to positive. Here these chemisorbed species may form neutral ion pairs within the Helmholtz layer act to offset the potential change.[42] This may explain why no significant excess charge is built up in the region where these surface redox reactions occur, and therefore results in an apparent potential region where minimum frequency changes occur(PRMF) that is situated between the C^+ and C^- zones.

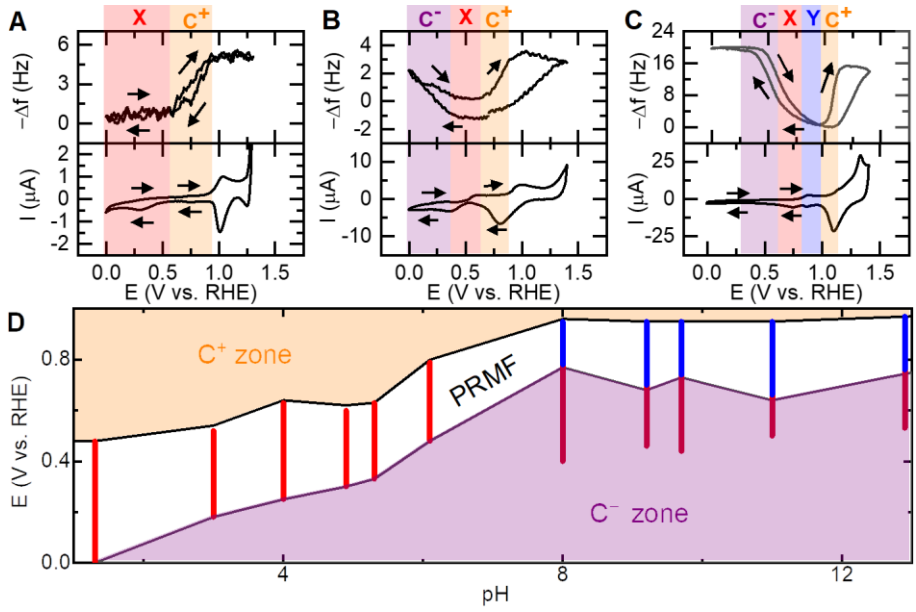

Fig. 6 Surface excess charge detection in different Ar-saturated pH solutions. (A-B) EQCM measurements on gold in 0.1M $HClO_4$ (**A**), $NaClO_4$ (**B**) and NaOH (**C**). The upper part displays the frequency response as a function of potential, while the lower part illustrates the CV. The scan rate is set at 50 mV/s in the EQCM measurements. The X and Y regions indicate the potential regions where the X and Y redox couples can be identified in a CV, respectively. C^+ signifies the potential region of positive excess charge, whereas C^- represents the potential region of negative excess charge. (**D**) Potential regions of C^+ and C^- observed across varying pH solutions. The red and blue lines depict the potential regions where the X and Y redox reactions are present, respectively, under Ar-saturated conditions. There is a potential region of minimum frequency (PRMF) between C^+ and C^- zones.

4.2.3 The electrified interface in the presence of oxygen

While discussions on electrochemical double layer (EDL) structure at electrode interfaces have persisted over a century,[23, 57, 58] the in situ visualization of the actual distribution of cations and anions at the solid-liquid interface during a catalytic process has remained elusive.[23, 59] Taking into account the linear correlation between $-\Delta f$ and ΔQ, and the hypothesis by Kautek

grouppoint to a potential region between C^+ and C^- where chemisorption occurs where frequency changes cannot be observed by EQCM, we can speculate what the charge distribution diagram at the solid-liquid interface would look like. While there may undoubtedly be more complex electrochemical processes at play at and near the PRMF, and we cannot dismiss the possibility that these other electrochemical processes also affect the excess free excess free charge and may not be detected by EQCM, in the following discussion we have assumed that the effect of such processes would be minimal. Under the assumption that $-\Delta f$ changes directly correlate with the excess charge, we can probe the EDL structure during catalytic processes. Since the oxygen reduction reaction (ORR) occurs within the PRMF region, we employed our EQCM methodology to detect the surface excess charge both under an inert atmosphere and during the catalytic ORR process.

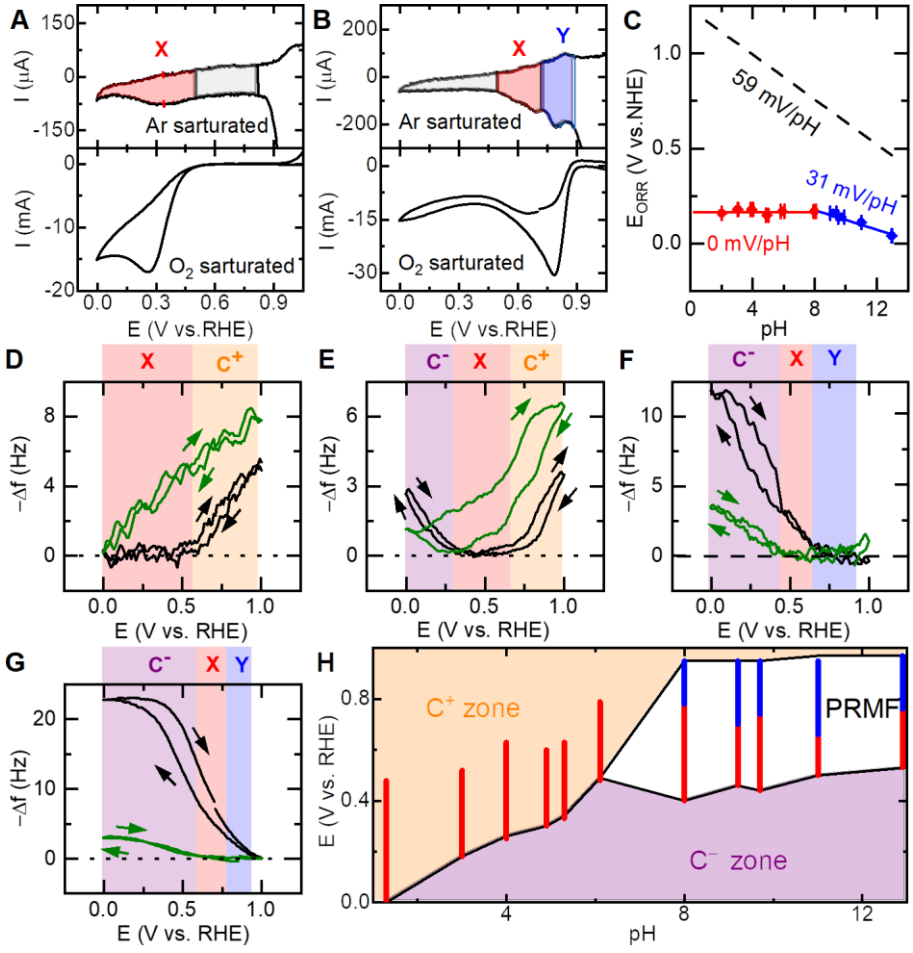

Fig. 7 Surface excess charge detection in the presence of oxygen reduction reaction in different pH solutions. (**A**) CVs of gold in Ar-saturated (top) and O_2-saturated (bottom) 0.1 M $HClO_4$ at 50 mV/s. (**B**) CVs of gold in Ar-saturated (top) and O_2-saturated (bottom) 0.1 M NaOH at 50 mV/s. **(C)** Pourbaix diagram illustrating the peak potential of oxygen reduction reaction (E_{ORR}) across the entire pH scale. (**D-G**) The EQCM frequency response in Ar-saturated (black line) and O_2-saturated (green line) conditions across different pH solutions: pH 1 (**D**), pH 4 (**E**), pH 10 (**F**), pH 13 (**G**). The X and Y zones indicate the potential regions where the X and Y redox couples are identifiable in a CV under Ar—saturated conditions. C^+ signifies the potential region of positive excess charge, while C^- represents the potential region of negative excess charge. (**H**) Potential regions of C^+ and C^- observed across varying pH solutions. The red and blue lines represent the potential regions where the X and Y redox reactions can be observed under Ar-saturated conditions, respectively.

Under saturated O_2 conditions, the potential region of the ORR consistently aligns with the potential regions where the X and Y redox reactions can be observed in the absence of O_2, as depicted in Fig. 7A and B. Given that the peak potential of the ORR, denoted as E_{ORR}, remains constant regardless of variations in the oxygen quantity, E_{ORR} apparently is not affected by kinetic factors, and therefore considered to be an interesting descriptor to monitor (Fig. S10). By recording E_{ORR} across different pH values and constructing a corresponding Pourbaix diagram (Fig. 7C), distinct E_{ORR} slopes (vs. NHE) become apparent. For pH levels lower than 8, E_{ORR} does not shift on the NHE reference scale. However, E_{ORR} displays a decrement of −31mV/pH once the pH surpasses 8. This dual E_{ORR} slope pattern in the Pourbaix diagram suggests that the rate−determining step of the electrochemical ORR process involves only electron transfer steps ($O_2 + e^- \rightleftarrows O_2^-$) within the pH range of 1-8, whereas it transitions to a two—electron and one−proton process ($O_2 + H^+ + 2e^- \rightleftarrows HO_2^-$) when the pH exceeds 8.

Gold, characterized by a weak oxygen binding energy, experiences a pronounced reduction in ORR overpotential when transitioning from acidic to alkaline solutions, a phenomenon akin to other materials exhibiting weak oxygen binding energies.[60] In terms of whether oxygen directly adsorb onto the catalyst, the ORR process can be conceptually divided into a surface-dependent inner-sphere electron transfer mechanism and a surface-independent

outer-sphere electron transfer mechanism.[61] Materials with low oxygen binding energies, including Au,[62] Ag,[63] carbon materials[64] and several oxides,[65] have been proposed to reduce O_2 through an outer-sphere electron transfer process. Within this context, it has been hypothesized that chemisorbed anions function as outer-sphere bridges between the O_2 and the Au surface, thereby stabilizing catalytic intermediates in alkaline solutions.[60, 62, 66] However, the outer-sphere electron transfer mechanism alone does not comprehensively explain the two distinct trends in ORR activities exhibited by these systems, occurring both below and above pH 8.

We conducted a comparatively analysis of the frequency response as a function of the applied potential using EQCM in both Ar−saturated and O_2−saturated solutions (Fig. 7D-G). When the pH of the solution is below 8, a notable difference is observed when comparing the conditions under saturated Ar and O_2. Specifically, the PRMF width diminishes, and the onset potential of C^+ zone, denoted as onset C^+ undergoes a negative potential shift under saturated O_2. (Fig. 7D and E). In instances where the pH is 1, the onset C^+ shifts from 0.55 V vs. RHE under Ar to 0 V vs. RHE under O_2 (Fig. 7D). Similarly, at pH 4, the onset C^+ transition occurs from 0.67 V vs. RHE under Ar to 0.3 V vs. RHE under O_2 (Fig. 7E). Moreover, EQCM analysis in presence of oxygen shows that the onset potential of the ORR falls within the C^+ region when the pH is below 8 (Fig. S11A and B).

Conversely, when the pH of the solution exceeds 8, a noticeable disparity of potential regions emerges in the PRMF and the C^- zone comparing saturated Ar and O_2. Notably, under O_2 ─saturated conditions, the PRMF consistently maintains its presence, even as the Faradaic current associated with catalytic O_2 reduction increases by a factor of 150 when compared to the current under Ar conditions (Fig. S11C and D). Moreover, its width expands in conjunction with the negatively shifted onset potential of the C^- zone, recognized as onset C^- (Fig. 7F and G).

Assuming that the variables resulting from the ORR reaction process, such as pH fluctuations and the quantities of reactants and products, have a minimal impact on the EQCM signal, the identification of the PRMF, C^+ and C^- zones within O_2─ saturated solutions becomes straightforward, as depicted in Fig. 7H. Any distinction can be easily observed when comparing conditions under O_2 (Fig. 7H) with that under Ar (Fig. 6D). Notably, when the pH is below 8,

the width of PRMF diminishes, and onset C^+ shifts negatively. Conversely, the width of PRMF expands, and the onset C^- shifts negatively when the pH exceeds 8. This notable change in the PRMF under O_2−saturated conditions could potentially imply that the presence of O_2 leads to the detachment of perchlorate from the electrode surface, while hydroxide remains bound.

In essence, the precise identification of the PRMF, C^+ and C^- zones reveals how the excess free charge may change under catalytic ORR conditions under the assumption that $-\Delta f$ changes directly correlate with the excess charge.

4.2.4 Charge distribution at electrified interfaces

The essence of the electrified interface lies in comprehending the distribution of the excess free charge. Assuming that Δf gives us the full picture regarding the surface excess charge, the processes occuring at the gold surface can be devided in a Faradaic process involving surface redox reactions in the PRMF, and non-Faradaic processes that occur in the C^- and C^+ zones. To assess these two processes, we examined the differential capacitances at varying pH, as depicted in Fig. 8A. Beyond the potential range of the surface redox reactions (X and Y zones), a differential capacitance of approximately 18 μF/cm^2 is observed. However, within the X and/or Y redox regions, the presence of charge transfer from chemical adsorption/desorption enhances the differential capacitance, resulting in a bell-shaped curve with a maximum capacitance of 50 μF/cm^2. The bell-shaped differential capacitance arises from the chemisorption of perchlorate (X region) and hydroxide (Y region) on gold. The chemical adsorption/desorption of perchlorate within the pH rang of 1-8 (Fig. 8B) and hydroxide within pH 8-13 (Fig. 8C) constitute two distinct surface redox reactions. We speculate that these surface reactions apparently impede the buildup of excess charge, resulting in the appearance of a PRMF where $-\Delta f$ remains minimal in EQCM experiments. This may suggest that excess charge is established and augmented only after the completion of chemical adsorption (during a positive scan) or desorption (during a negative scan) (Fig. 8D).

To analyze the net Faradaic charge distribution of surface redox reactions existing in the PRMF, we sum the integrated charge of adsorption during positive and desorption during negative scan in a CV experiment (Section S3 (2) and Fig.S12). For the non-Faradaic regions

(i.e. the C^+ and C^- zones), we can calculate the accumulated excess charge (ΔQ) using the potential difference (ΔE) between the onset potential of the non-Faradaic region to the calculated potential point, as well as the known capacitance (C_{Ar}) from a cyclic voltammogram (Fig. 8A). The formula for calculating ΔQ is $\Delta Q = \frac{C_{Ar} \times \Delta E}{A}$, where A is the electrode surface area (section S3(3)). By plotting the calculated Faradaic charge in the PRMF area and the excess charge in the non-Faradaic zones as a function of the applied potential, we can construct excess free charge distribution diagrams that are based on our assumption that Δf relates directly to the surface excess charge. (Fig. 8E-F).

Determination of the distribution of excess charge during a catalytic process where significant catalytic currents can be observed, has been unprecedented due to the lack of appropriate methods. Our EQCM methodology allows for the exploration of the excess charge by monitoring the frequency response during the catalytic oxygen reduction process. While it is not feasible to measure the excess charge directly from current under catalytic conditions, we managed to estimate the capacitance within O_2-saturated solutions by utilizing the relationship between the frequency changes and the excess free charge. Based on the linear relationship between the frequency changes observed by EQCM to the excess free charge, we speculate that the slope of these frequency changes as a function of the potential change is linked to capacitance through the equation $C = \frac{Q}{\Delta E} \propto \frac{-\Delta f}{\Delta E}$ (Fig. S13). Assuming that the reactants and products in a catalytic process do not significantly influence the frequency of the EQCM, we can obtain the difference in capacitance between an O_2 and an Ar atmosphere, which can be related using a corrective coefficient (K). This coefficient is calculated as the ratio of $\frac{-\Delta f}{\Delta E}$ under O_2 to the that recorded under Ar and is expressed as $K = \frac{(\frac{-\Delta f}{\Delta E})_{O_2}}{(\frac{-\Delta f}{\Delta E})_{Ar}} = \frac{C_{O_2}}{C_{Ar}}$.

By comparing the frequency response under O_2 and under Ar, it becomes clear that K correlates linearly with E within the C^- zone, while K is unaffected by E in the C^+ zone (Fig. S13). This disparity is due to $(\frac{-\Delta f}{\Delta E})_{O_2}$ not being fully linear in contrast to $(\frac{-\Delta f}{\Delta E})_{Ar}$. The observed disparity can likely be attributed to the occurrence of the ORR, which takes place prominently in the PRMF and C^- zone but is less prevalent in the C^+ zone. Since K remains constant at 0.8

in the C^+ zone (Fig. S13C), we assume the excess charge in the C^+ zone under O_2 saturated conditions using the equation $\Delta Q_{O_2} == \frac{0.8\, C_{Ar} \times \Delta E}{A}$. The determination of capacitance in the C^- zone under O_2 conditions can be determined, and relies on the corrective coefficient K expressed as $C_{O_2} = K \times C_{Ar}$, wherein K was found emperically to change with $K = 0.18 - 0.24 \times E$ (More details in Fig. S13 and section S4). Consequently, we can estimate the excess charge in the C^- and C^+ zones, respectively, thereby unveiling a qualitative excess charge distribution diagram under saturated O_2 conditions as well. (Fig. 8G) Assuming excess free charge is reflected by the frequency changes of EQCM, the diagram visually demonstrates how the excess charge may fluctuate as a function of pH and the applied potential before and during catalysis.

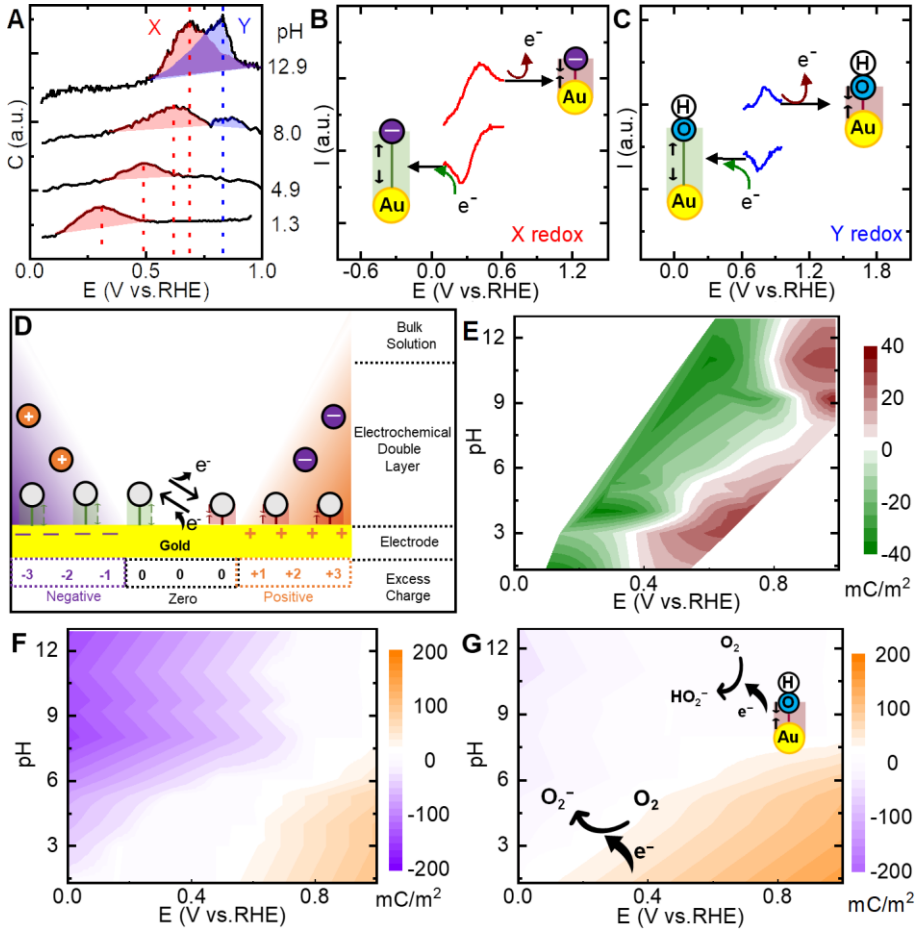

Fig. 8 Proposed charge distribution diagram on the gold surface in a full pH scale. (**A**) Average differential capacitances (C) calculated by cyclic voltammetry as a function of pH, with a potential range of 0 – 1 V vs. RHE and scan rate of 0.05 V/s. The pH of the solutions is adjusted using a mixture of 0.1 M $HClO_4$, $NaClO_4$ and NaOH. (More calculation details are shown in Section S3(1)). The red X and blue Y regions illustrate the contribution of ClO_4^- and OH^- surface redox reactions to the increase in the capacitance of gold. (**B**) Proposed X redox reaction (ClO_4^- chemical adsorption/desorption) on the gold surface. The red line represents a segment of the CV involving the X redox reaction. (**C**) Proposed Y redox reaction (OH^- chemical adsorption/desorption) on the gold surface. The blue line represents a segment of the CV involving the Y redox reaction. (**D**) Proposed structure of the electric double layer (EDL) on gold. The surface excess charge changes from negative (purple) to neutral and positive (orange) as the applied potential increases. Dark green and dark red boxes represent the chemical desorption and adsorption on the surface, respectively. (**E**) Distribution diagram of the net Faradaic charge for specific adsorption/desorption involving electron transfer in an Ar-saturated environment. The net charge of the surface redox reactions is the sum of integrated charges from both the positive and negative scans. (More details are shown in Section S3(2) and Fig.S12). (**F**) Surface excess charge distribution diagram on gold as a function of the pH under an Ar─saturated solution, within the potential region of 0 ─ 1 V vs. RHE. Purple, white, and orange colors represent three distinct excess charge states of the gold surface: negative, neutral, and positive, respectively. The details of mathematical model of excess charge under saturated Ar conditions are provided in Section S2(3). (**G**) Surface excess charge distribution diagram on gold as a function of pH in O_2-saturated solutions, within the potential region of 0-1 V vs. RHE. Purple, white, and orange colors represent three distinct excess charge states of the gold surface: negative, neutral, and positive, respectively. Further details of the mathematical model of excess charge under saturated O_2 conditions are discussed in Section S4.

4.3 Conclusion

In summary, our study presents a methodology for exploring the excess free charge by EQCM. Through the analysis of three distinct frequency responses of a quartz crystal, we have

successfully identified the potential regions where significant excess charge builds up on the electrode, i.e. a positive excess charge concentrated in the C^+ zone and a negative excess charge localized in the C^- zone. Additionally, we pinpointed an apparent potential region of where frequency changes cannot be detected by EQCM (PRMF), and where surface redox reactions involving Faradaic charge transfer are occurring. This EQCM method appears to be very versatile even during the electrocatalytic ORR. Moreover, our comprehensive EQCM and CV analysis has allowed us to create informative excess free charge distribution diagrams. These insights not only allow us to enhance our understanding of the interface environment in various materials, but also lay the groundwork for future investigations into tracking the real excess free charge dynamics during diverse chemical processes. Since the principles underlying a $-\Delta f$ response as a function of ΔQ are not understood, and the precise reason for the absence of a frequency response in the PRMF remains unknown, it is worthwhile to conduct further investigations into these precise phenomena. This can be achieved through a comparative analysis of different in situ methods and the application of more detailed mathematical models.

4.4 References

1. Jeanmairet, G.; Rotenberg, B.; Salanne, M., *Chem Rev* **2022,** *122* (12), 10860-10898.
2. Schmickler, W., *Chemical Reviews* **1996,** *96* (8), 3177-3200.
3. Lin, S.; Chen, X.; Wang, Z. L., *Chem Rev* **2022,** *122* (5), 5209-5232.
4. Noori, A.; El-Kady, M. F.; Rahmanifar, M. S.; Kaner, R. B.; Mousavi, M. F., *Chem Soc Rev* **2019,** *48* (5), 1272-1341.
5. Le, J.-B.; Fan, Q.-Y.; Li, J.-Q.; Cheng, J., *Science Advances* **2020,** *6* (41), eabb1219.
6. Velasco-Velez, J.-J.; Wu, C. H.; Pascal, T. A.; Wan, L. F.; Guo, J.; Prendergast, D.; Salmeron, M., *Science* **2014,** *346* (6211), 831-834.
7. Le, J.; Iannuzzi, M.; Cuesta, A.; Cheng, J., *Phys Rev Lett* **2017,** *119* (1), 016801.
8. Frumkin, A. N.; Petrii, O. A., *Electrochim. Acta* **1975,** *20* (5), 347-359.
9. Chen, J.; Nie, L.; Yao, S., *Journal of Electroanalytical Chemistry* **1996,** *414* (1), 53-59.
10. Ojha, K.; Doblhoff-Dier, K.; Koper, M. T. M., *Proc Natl Acad Sci U S A* **2022,** *119* (3).
11. Payne, R., Double Layer at the Mercury-Solution Interface. In *Progress in Surface and Membrane Science*, Danielli, J. F.; Rosenberg, M. D.; Cadenhead, D. A., Eds. Elsevier: 1973; Vol. 6, pp 51-123.
12. Doblhoff-Dier, K.; Koper, M. T. M., *The Journal of Physical Chemistry C* **2021,** *125* (30), 16664-16673.
13. Rizo, R.; Sitta, E.; Herrero, E.; Climent, V.; Feliu, J. M., *Electrochim. Acta* **2015,** *162*, 138-145.
14. Weaver, M. J., *Langmuir* **1998,** *14* (14), 3932-3936.
15. Sarabia, F. J.; Sebastián, P.; Climent, V.; Feliu, J. M., *Journal of Electroanalytical Chemistry* **2020,** *872*.
16. Climent, V.; Coles, B. A.; Compton, R. G., *The Journal of Physical Chemistry B* **2002,** *106* (20), 5258-5265.
17. Ryu, J.; Surendranath, Y., *J Am Chem Soc* **2019,** *141* (39), 15524-15531.
18. Martínez-Hincapié, R.; Climent, V.; Feliu, J. M., *Electrochemistry Communications* **2018,** *88*, 43-46.
19. Xu, P.; von Rueden, A. D.; Schimmenti, R.; Mavrikakis, M.; Suntivich, J., *Nat Mater* **2023**.
20. Marinković, N. S.; Calvente, J. J.; Kloss, A.; Kováčová, Z.; Ronald Fawcett, W., *Journal of Electroanalytical Chemistry* **1999,** *467* (1), 325-334.
21. Magnussen, O. M., *Chemical Reviews* **2002,** *102* (3), 679-725.
22. Lu-Lu Zhang, C.-K. L., Jun Huang, *Journal of Electrochemistry* **2022,** *28* (2), 2108471.
23. Huang, J., *JACS Au* **2023,** *3* (2), 550-564.
24. Wang, X.; Kuang, Y.; Le, J.-B., *Current Opinion in Electrochemistry* **2023,** *40*.
25. Zhang, M.-K.; Cai, J.; Chen, Y.-X., *Current Opinion in Electrochemistry* **2022,** *36*.
26. Li, C. Y.; Le, J. B.; Wang, Y. H.; Chen, S.; Yang, Z. L.; Li, J. F.; Cheng, J.; Tian, Z. Q., *Nat Mater* **2019,** *18* (7), 697-701.
27. Li, X. Y.; Jin, X. F.; Yang, X. H.; Wang, X.; Le, J. B.; Cheng, J., *J Chem Phys* **2023,** *158* (8), 084701.
28. Le, J. B.; Chen, A.; Li, L.; Xiong, J. F.; Lan, J.; Liu, Y. P.; Iannuzzi, M.; Cheng, J., *JACS Au* **2021,** *1* (5), 569-577.
29. Tian, Z.-Q.; Ren, B.; Chen, Y.-X.; Zou, S.-Z.; Mao, B.-W., *Journal of the Chemical Society, Faraday Transactions* **1996,** *92* (20), 3829-3838.
30. Monteiro, M. C. O.; Dattila, F.; Hagedoorn, B.; García-Muelas, R.; López, N.; Koper, M. T. M., *Nat. Catal.* **2021,** *4* (8), 654-662.
31. Shah, A. H.; Zhang, Z.; Huang, Z.; Wang, S.; Zhong, G.; Wan, C.; Alexandrova, A. N.; Huang, Y.; Duan, X., *Nat. Catal.* **2022,** *5* (10), 923-933.
32. Gu, J.; Liu, S.; Ni, W.; Ren, W.; Haussener, S.; Hu, X., *Nat. Catal.* **2022,** *5* (4), 268-276.
33. Strmcnik, D.; Kodama, K.; van der Vliet, D.; Greeley, J.; Stamenkovic, V. R.; Marković, N. M., *Nat. Chem.* **2009,** *1* (6), 466-472.
34. Luo, M.; Koper, M. T. M., *Nat. Catal.* **2022,** *5* (7), 615-623.
35. Tang, B. Y.; Bisbey, R. P.; Lodaya, K. M.; Toh, W. L.; Surendranath, Y., *Nat. Catal.* **2023,** *6* (4), 339-350.
36. Simon, P.; Gogotsi, Y.; Dunn, B., *Science* **2014,** *343* (6176), 1210-1211.
37. Brousse, T.; Bélanger, D.; Long, J. W., *Journal of The Electrochemical Society* **2015,** *162* (5), A5185-A5189.
38. Simon, P.; Gogotsi, Y., *Nature Materials* **2008,** *7* (11), 845-854.
39. Hubkowska, K.; Łukaszewski, M.; Czerwiński, A., Quartz crystal nanobalance measurements in electrocatalysis. In *Encyclopedia of Interfacial Chemistry*, Wandelt, K., Ed. Elsevier: Oxford, 2018; pp 402-412.
40. Boer, D. D.; Siberie, Q.; Siegler, M. A.; Ferber, T. H.; Moritz, D. C.; Hofmann, J. P.; Hetterscheid, D. G. H., *ACS Catal.* **2022,** *12* (8), 4597-4607.
41. Daikhin, L.; Gileadi, E.; Tsionsky, V.; Urbakh, M.; Zilberman, G., *Electrochim. Acta* **2000,** *45* (22), 3615-3621.
42. Kautek, W.; Sahre, M.; Soares, D. M., *Ber. Bunsenges. Phys. Chem.* **1995,** *99* (4), 667-676.
43. Watanabe, M.; Uchida, H.; Ikeda, N., *J. electroanal. chem.* **1995,** *380* (1), 255-260.
44. Hetterscheid, D. G. H., *Chem Commun (Camb)* **2017,** *53* (77), 10622-10631.
45. Tsai, W. Y.; Taberna, P. L.; Simon, P., *J Am Chem Soc* **2014,** *136* (24), 8722-8.
46. Levi, M. D.; Sigalov, S.; Salitra, G.; Elazari, R.; Aurbach, D., *J Phys Chem Lett* **2011,** *2* (2), 120-4.

47. Levi, M. D.; Levy, N.; Sigalov, S.; Salitra, G.; Aurbach, D.; Maier, J., *Journal of the American Chemical Society* **2010,** *132* (38), 13220-13222.
48. Edens, G. J.; Gao, X.; Weaver, M. J., *Journal of Electroanalytical Chemistry* **1994,** *375* (1), 357-366.
49. Zhumaev, U. E.; Lai, A. S.; Pobelov, I. V.; Kuzume, A.; Rudnev, A. V.; Wandlowski, T., *Electrochim. Acta* **2014,** *146*, 112-118.
50. Garlyyev, B.; Xue, S.; Watzele, S.; Scieszka, D.; Bandarenka, A. S., *J Phys Chem Lett* **2018,** *9* (8), 1927-1930.
51. Schmickler, W.; Guidelli, R., *Electrochim. Acta* **2014,** *127*, 489-505.
52. Štrbac, S.; Adžić, R. R., *Journal of Electroanalytical Chemistry* **1996,** *403* (1), 169-181.
53. Prieto, A.; Hern&#xfffd;ndez, J.; Herrero, E.; Feliu, J. M., *Journal of Solid State Electrochemistry* **2003,** *7* (9), 599-606.
54. Costentin, C.; Porter, T. R.; Saveant, J. M., *ACS Appl Mater Interfaces* **2017,** *9* (10), 8649-8658.
55. Yang, X.; Rogach, A. L., *Advanced Energy Materials* **2019,** *9* (25).
56. Elgrishi, N.; Rountree, K. J.; McCarthy, B. D.; Rountree, E. S.; Eisenhart, T. T.; Dempsey, J. L., *Journal of Chemical Education* **2018,** *95* (2), 197-206.
57. Doblhoff-Dier, K.; Koper, M. T. M., *Current Opinion in Electrochemistry* **2023**.
58. Pajkossy, T.; Kolb, D. M., *Electrochemistry Communications* **2003,** *5* (4), 283-285.
59. Damaskin, B. B.; Petrii, O. A., *Journal of Solid State Electrochemistry* **2011,** *15* (7-8), 1317-1334.
60. Ramaswamy, N.; Mukerjee, S., *Advances in Physical Chemistry* **2012,** *2012*, 1-17.
61. Ramaswamy, N.; Mukerjee, S., *The Journal of Physical Chemistry C* **2011,** *115* (36), 18015-18026.
62. Ignaczak, A.; Santos, E.; Schmickler, W., *Current Opinion in Electrochemistry* **2019,** *14*, 180-185.
63. Blizanac, B. B.; Ross, P. N.; Markovic, N. M., *Electrochim. Acta* **2007,** *52* (6), 2264-2271.
64. Yang, H. H.; McCreery, R. L., *Journal of The Electrochemical Society* **2000,** *147* (9), 3420.
65. Shao, M.; Chang, Q.; Dodelet, J. P.; Chenitz, R., *Chem Rev* **2016,** *116* (6), 3594-657.
66. Duan, Z.; Henkelman, G., *ACS Catalysis* **2019,** *9* (6), 5567-5573.